Real-Time Vessel Segmentation and Tracking for Ultrasound Imaging Applications

Julian Guerrero*, *Student Member, IEEE*, Septimiu E. Salcudean, *Fellow, IEEE*, James A. McEwen, *Member, IEEE*, Bassam A. Masri, and Savvakis Nicolaou

***Abstract*—A method for vessel segmentation and tracking in ultrasound images using Kalman filters is presented. A modified Star–Kalman algorithm is used to determine vessel contours and ellipse parameters using an extended Kalman filter with an elliptical model. The parameters can be used to easily calculate the transverse vessel area which is of clinical use. A temporal Kalman filter is used for tracking the vessel center over several frames, using location measurements from a handheld sensorized ultrasound probe. The segmentation and tracking have been implemented in real-time and validated using simulated ultrasound data with known features and real data, for which expert segmentation was performed. Results indicate that mean errors between segmented contours and expert tracings are on the order of 1%–2% of the maximum feature dimension, and that the transverse cross-sectional vessel area as computed from estimated ellipse parameters a, b as determined by our algorithm is within 10% of that determined by experts. The location of the vessel center was tracked accurately for a range of speeds from 1.4 to 11.2 mm/s.**

***Index Terms*—Deep venous thrombosis, image segmentation, Kalman filtering, ultrasound, vessel tracking.**

I. Introduction

ULTRASOUND is a widely used medical imaging modality. It is inexpensive, widely accessible, fast, and safe. Ultrasound image segmentation is required in a number of medical examinations. For example, in obstetrics, dimensions of various anatomical features of the fetus must be measured; in oncology, the prostate must be outlined for radiation treatment planning; in cardiovascular applications, deep venous thrombosis (DVT) and atherosclerosis are diagnosed using segmented features in ultrasound images. However, image segmentation is made difficult by shadowing and speckle typical of ultrasound images [1].

In DVT, blood clots or thrombi are formed within the deep veins. These thrombi may occlude venous flow, or break off from the vessel wall and cause a possibly fatal pulmonary embolism. It has been reported that there are from 170 000 to as many as 260 000 patients diagnosed and treated each year in the United States [2], and the annual incidence of a first episode of clinically suspected venous thrombosis has been estimated at 2%–4% in the general population [3].

The diagnosis of DVT is primarily done through compression ultrasound (CUS) examinations [4]. The examiner applies gentle ultrasound transducer pressure while imaging a region of interest, and the imaged vein collapses unless there is a thrombus inside [5], [6]. Since younger thrombi and blood have similar echogenicity it may not be possible to identify a thrombus from a single image, and it is necessary for the examiner to press down and observe the sequence of B-mode images to determine the presence or absence of thrombi. Chronic thrombi may be more echogenic, but for DVT treatment it is important that a decision be made early during thrombus formation.

A high operator dependence has been reported for CUS examinations [7], [8]. Single limb screenings may take in excess of 40 minutes and repeat scans have been reported in up to 76% of cases [9]. A "single ultrasound" examination strategy for DVT detection has been suggested [10]–[12] addressing these concerns. Schellong *et al.* [11] present a methodology that includes the strict standardization of the ultrasound examination protocol and a sound training of the sonographer. The authors argue that by making the examination more objective (standardization of the examination) and by reducing user variability (sound ultrasonographer training), the diagnostic workup of patients can be reduced to a single examination. Image segmentation may be a means for achieving a standardization of the examination.

Segmentation methods that incorporate knowledge about the shape or geometry of the desired feature may improve detection. A broad review of ultrasound segmentation methods has been presented in [1], which focuses on B-mode imaging and specific clinical application areas [echocardiography, breast ultrasound, transrectal ultrasound (TRUS), and intravascular ultrasound (IVUS)], and where multiple methods that use assumed feature geometry are presented.

In [1], segmentation methods were classified based on whether the output was a detected contour or curve, or a grouping of pixels into regions, among other criteria such as dimensionality of the data. In the 2-D domain, multiple contour finding approaches are based on the active contours concept, where the contour location is determined by balancing "forces" obtained from processed image data and counteracting local constraints determined by the active contour model. Models based on active contours or snakes [13], [14] are among the most prominent methods in the field for image segmentation. However, these methods have the drawback that they require

Manuscript received January 15, 2007; revised April 25, 2007. This work was supported by the Natural Sciences and Engineering Research Council of Canada (NSERC). *Asterisk indicates corresponding author*.

*J. Guerrero is with the Department of Electrical and Computer Engineering, University of British Columbia, Vancouver, BC V6T 1Z4, Canada.

S. E. Salcudean and J. A. McEwen are with the Department of Electrical and Computer Engineering, University of British Columbia, Vancouver, BC V6T 1Z4, Canada.

B. A. Masri is with the Department of Orthopaedics, University of British Columbia, Vancouver, BC V5Z 4E3, Canada.

S. Nicolaou is with the Department of Radiology, University of British Columbia, Vancouver, BC V5Z 4E3, Canada.

Digital Object Identifier 10.1109/TMI.2007.899180

careful initialization, are difficult to implement in real-time, and often require careful tuning of parameters for convergence.

Many authors have attempted to determine contours from various types of vessels in ultrasound images, some of which were reviewed in [1]. While IVUS depicts vessels, several key differences exist between IVUS images and the deep vein images obtained during a compression examination. The geometry of IVUS images is described in polar coordinates, while linear arrays are typically used for CUS exams. Also, the range of isonation frequencies for IVUS is 30–40 MHz, while CUS exams use arrays at 4–10 MHz, resulting in clear differences in image scale, resolution, and depth. Methods used for segmenting vessels in IVUS cannot, therefore, be directly applied to segmentation of the deep vessels of the lower limb.

Segmenting vessels, namely the carotid artery, in images from linear arrays has been addressed by [15]–[18], among others. In [15] and [16] a model-based ultrasound segmentation algorithm is presented. A Star–Kalman algorithm uses a circular vessel model to detect vessel boundaries in ultrasound images of the carotid artery, as explained in more detail in Section III. In [17], a discrete dynamic contour model is used to determine the lumen contour of the carotid artery by internal forces calculated from geometrical properties of the contour, and by external forces obtained from the image gray level features. The algorithm is initialized by a single seed point, and the image gradient and the local gray level ratio between the inside and outside of the contour are combined to calculate the external forces. Good results are reported, but algorithm robustness depends on the quality of training images used to obtain algorithm parameters. Another deformable model based method uses a modified balloon model [18]. In this case, a combination of the gradient and the second order derivative of the image is used as the external force, while an internal "pressure" is used to push the boundary outward. A 3-D arterial model was constructed using the extracted contours. Good results are also reported for carotid artery images.

Also addressed in [1] is the use of filters in order to improve segmentation. Other examples include filtering of ultrasound images by low pass filters [19] and median filters [20].

When tracking features in ultrasound images over several frames, template matching is a common procedure; the feature to be detected is described by a mask and a correlation procedure is performed to determine its location. The work of [21] presents a comparison of different correlation methods to track speckle motion using sum of absolute differences (SAD), normalized and nonnormalized correlation, resulting in similar performance characteristics. The work of [22] also used SAD to track ultrasound speckle patterns to determine blood flow velocity and angle in carotid arteries, and state that "SAD methods proved to be the most efficient measure with virtually identical performance to other explored methods." Drawbacks to these types of methods include high processing requirements.

Others [15] have used Kalman filters for tracking a seed point in real-time ultrasound images. The movement of the seed point through space is described by a dynamic model and measurements are used to estimate the position of the point.

This paper presents the image segmentation and tracking developed for a new CUS approach to the detection of DVT. The overall approach has been presented in [23], with the goal of making the CUS examination less operator dependent and faster in two ways: by obtaining objective measures of venous compressibility and by recording 3-D venous compressibility maps automatically. The work of [23] only summarizes the vein segmentation approach from ultrasound images, which is the basis for obtaining the examination objective measures. The segmentation approach is described here, where the model description is provided in sufficient detail for implementation and comparison to other methods, and the segmentation is characterized by using synthesized images and patient images. In addition, this paper describes the temporal Kalman filter used to track the feature location over successive image frames.

The paper is organized as follows. Section II presents an overview of previous work on a CUS screening system and the instrumentation of the ultrasound transducer as presented in [23]. Section III presents in detail the approach taken for vessel segmentation, while Section IV presents the vessel tracking. Section V presents the validation protocol, while Section VI presents experimental results. A discussion follows in Section VII, with the conclusion in Section VIII.

II. DVT Screening With Compression Measures

The work of [23] presents a DVT screening system, including the development and validation of objective measures for CUS, the development of the sensing system, and the construction and graphical rendering of the vein models built from segmented vessels. In that approach, the transverse vessel area is approximated and used in conjunction with measurements of the force applied by the ultrasound transducer and transducer location to calculate vessel compressibility measures. Veins are segmented in cross-sectional ultrasound images in real-time, with framerates of 10–16 Hz and better, and the feature location is tracked over successive image frames using a temporal Kalman filter and location measurements from an electromagnetic position sensor attached to the ultrasound transducer.

The system instrumentation for the DVT screening system is described in detail in [23], and is only summarized here for completeness. The system consists of 1) a PC-based ultrasound machine (RP 500, Ultrasonix Medical Corporation, Richmond, BC, Canada), 2) a sensorized handheld transducer that includes 6 degree-of-freedom (6DOF) localization using a magnetic sensor (PCIBird, Ascension Technology Corporation, Burlington, VT) and a 6DOF force/torque sensor (Nano25, ATI Industrial Automation, Inc., Apex, NC) that monitors the forces applied to tissue, and 3) a user interface that connects the segmented vessel contours into single tubular structures and renders them to the user, color-coded with a measurement-based vein compressibility measure. Image acquisition is performed using the libraries provided by Ultrasonix. These allow direct access to memory and image data at the native ultrasound frame rate, and no additional video acquisition hardware is necessary.

To measure transducer forces, two rigid shells were constructed to surround the linear 9–4 MHz ultrasound probe. The inner shell is fixed to the probe, while the outer shell is connected to the inner shell through the force/torque sensor at

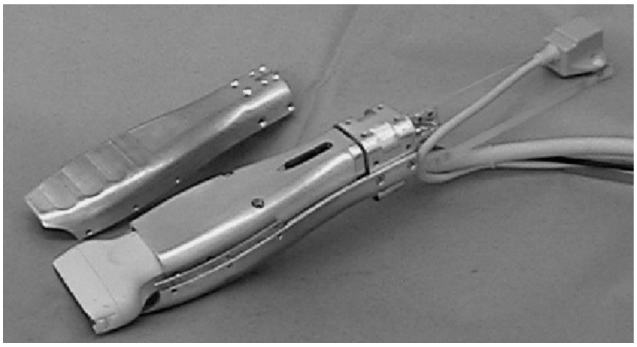

Fig. 1. Sensorized ultrasound probe used in the DVT screening system shown, where the outer shell surrounds the ultrasound probe and inner shell. Inner and outer shells are connected at the rear by a force/torque sensor, and a location sensor is mounted on a Plexiglas rod.

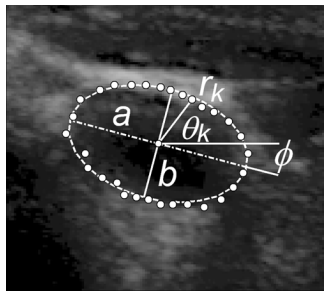

Fig. 2. Ellipse model for transverse vessel area. A vessel contour in an ultrasound image can be approximated by using an elliptical model with parameters a, b, and ϕ. Each contour point can be described in polar coordinates by $r_k = f(a, b, \phi, \theta_k)$.

the rear, as shown in Fig. 1. The examiner can then grasp and manipulate the ultrasound probe in a regular manner, and all applied forces and torques are acquired. The location of the probe is obtained by rigidly attaching the electromagnetic sensor to the rear of the outer shell by a 130-mm-long Plexiglas rod. The locations of the image plane and extracted 2-D contours with respect to a common 3-D reference frame are calculated using a calibrated homogeneous transformation and the location measurements. Many authors have reported successfully using electromagnetic sensors in this manner [24] and reported errors for these types of systems have been low (close to or less than 1% of the dimension of interest) [25], and are considered small enough not to interfere with the present application.

The DVT screening system requires a vessel segmentation method that can detect vessel contours and provide an estimate of the transverse vessel area from ultrasound images in real-time. In [23], the contour detection algorithm presented in Section III is used. Estimated ellipse parameters and the final search area from one image are used to initialize the contour detection in the following image frame. In addition, the vessel is tracked from frame to frame, as described in Section IV.

The estimates of the transverse vessel area are used to calculate two vessel compressibility measures to determine the possibility of DVT within the examined vessel. The first DVT likelihood measure is called the transverse area ratio (TAR), which is the ratio of minimum to maximum transverse vessel area of a vessel segment, obtained as an examiner presses down and then retracts the ultrasound probe. A healthy vessel is expected to compress completely, generating a TAR close to 0%, while it is expected that a diseased vessel will not ($\mathrm{TAR} \simeq 100\%$). The second measure is the slope of the line fit to the normalized calculated transverse areas as a function of the normalized applied force for a vessel segment. The slope corresponding to a healthy vein would have a value close to -1, while the presence of a thrombus would be indicated by a value close to 0.

A 3-D model is constructed using the estimated vessel contours, and the vessel compressibility measures are mapped to the vessel model surface as a color map and displayed to the user.

III. Vessel Segmentation

A real-time method for identifying the carotid artery contour in cross-sectional ultrasound images was presented in [15] and [16]. Using a Star algorithm [19] and a Kalman filter, the algorithm assumes that the underlying vessel contour is a circle. Starting with a seed point inside the carotid artery, intensity data is detected along radii distributed uniformly in a star shape. The most probable location of the vessel lumen is detected based on a probabilistic edge detection function. The distance from the seed point to the detected vessel lumen is treated as the measurement in a spatial Kalman filter having the radius as a function of radius angle as a state. No parameters need to be identified in this algorithm, as the Kalman filter dynamics simply state that the radius is a constant as a function of radius angle. This algorithm has been shown to perform well in detecting features even with echo drop-outs and shadowing artifacts.

Although the above circular model is adequate for arteries, in the case of a vein under compression the assumption that the vessel contour is a circle does not always hold. We propose an elliptical model to describe the contour of the vein and approximate the vessel area in a cross-sectional ultrasound image. In polar coordinates from the center of the ellipse, the ellipse radius r is given as a function of the radius angle θ by

$$r = \frac{a\,b}{\sqrt{b^2\,\cos^2(\theta-\phi) + a^2\,\sin^2(\theta-\phi)}} \tag{1}$$

where the parameters ϕ, a, and b are the angle and the length of the semi-major axis, and the length of the semi–minor axis, respectively, as shown in Fig. 2.

An uncompressed vein is described by an ellipse with eccentricity $e = \sqrt{1 - b^2/a^2} \approx 0$ which resembles a circle, while a heavily compressed vein can be described using an ellipse with an eccentricity value $e \sim 1$. In order to follow the approach from [15] and [16], knowledge of the ellipse parameters are required to formulate spatial Kalman filter dynamics describing the ellipse radius length as a function of the radius angle. Alternatively, the ellipse parameters can be included in an extended Kalman filter and are estimated from measurement data. This is the approach taken by the authors.

The use of an ellipse is a convenient way in which to model the global information of the vessel contour, including varying aspect ratios and orientations. It was selected because it is a smooth curve described by few parameters, and provides a quick way to compute the approximate enclosed area. In many cases, compressed veins will be accurately approximated by ellipse,

while in others this approximation will have significant errors. *However, the use as an ellipse as the global model is not crucial for the contour detection algorithm to provide small approximation errors, because the ellipse model is used primarily to provide the a good search bracket for the edge detection algorithm, and not to parameterize the edge.*

The segmentation is achieved by acquiring an ultrasound image of a vein seen on the transverse plane, and a *seed point* (x_c, y_c) is selected, as described in Section IV, inside the contour of the desired vessel. N angularly equispaced radii are then projected from the seed point to a maximum search distance $r_{\max}$, which must be larger than the feature to be detected. $r_{\max}$ is calculated from the assumed maximum vessel size and the known image scaling factors. Alternately, the vessel size in pixels can be used. In our studies, vessel size was found to be approximately 10 mm [23] and image scaling factors for our DVT screening system range from 0.069 to 0.2 mm/pix. An extended Kalman filter then generates estimates of the edge location $\hat{r}$, and the ellipse parameters $\hat{a}$, $\hat{b}$, $\hat{\phi}$.

The nonlinear system describing the ellipse radius in terms of the ellipse parameters from (1) can be written as

$$\begin{cases} \boldsymbol{x}_{k+1} = \boldsymbol{x}_k + \boldsymbol{\xi}_k \\ r_k = C(\boldsymbol{x}_k) + \eta_k \end{cases} \tag{2}$$

where

$$C(\boldsymbol{x}_k) = \frac{a_k\, b_k}{\sqrt{b_k^2\, \cos^2(\theta_k - \phi_k) + a_k^2\, \sin^2(\theta_k - \phi_k)}} \tag{3}$$

the state is $\boldsymbol{x}_k = [a_k, b_k, \phi_k]^\top$, $k = 1$ to N is a radius angle index, $\theta_k = 2\pi k/N$, and $\boldsymbol{\xi}_k$ and η_k are assumed to be sequences of white, zero-mean, Gaussian process and measurement noise, respectively, with constant covariances $\boldsymbol{Q}$ and R, respectively. The output r_k is the radius length from the seed point to the vessel boundary at angle θ_k and a function of the parameters a_k, b_k and ϕ_k.

The framework of nonlinear state estimation using extended Kalman filters [26] is used to find the state estimate $\hat{x}_k$ using the model defined by (2). The estimate $\hat{x}_{k|k}$ of the state x_k is obtained from

$$\hat{\boldsymbol{x}}_{k|k} = \hat{\boldsymbol{x}}_{k|k-1} + \boldsymbol{G}_k(r_k - C(\hat{\boldsymbol{x}}_{k|k-1})\,) \tag{4}$$

where $\boldsymbol{G}_k$ is the Kalman gain, and $\hat{\boldsymbol{x}}_{k|k-1} = \hat{\boldsymbol{x}}_{k-1|k-1}$. The Kalman gain for this system is obtained from

$$\boldsymbol{G}_k = \boldsymbol{P}_{k|k-1}\, \boldsymbol{H}_k^\top\, S_k^{-1} \tag{5}$$

where $\boldsymbol{P}_{k|k-1}$ is the state prediction covariance obtained from

$$\boldsymbol{P}_{k|k-1} = \boldsymbol{P}_{k-1|k-1} + \boldsymbol{Q} \tag{6}$$

S_k is the measurement prediction covariance obtained from

$$S_k = \boldsymbol{H}_k\, \boldsymbol{P}_{k|k-1}\, \boldsymbol{H}_k^\top + R \tag{7}$$

and $\boldsymbol{H}_k$ is defined as the Jacobian of $C(\hat{\boldsymbol{x}}_{k|k-1})$, or

$$\boldsymbol{H}_k \triangleq \left[\nabla_{\boldsymbol{x}} C(\boldsymbol{x})^\top\right]^\top \Big|_{\boldsymbol{x}=\hat{\boldsymbol{x}}_{k|k-1}} \tag{8}$$

which is at the core of the extended Kalman filtering procedure, and effectively linearizes the system [26]. The state covariance is updated using

$$\boldsymbol{P}_{k|k} = \boldsymbol{P}_{k|k-1} - \boldsymbol{G}_k\, S_k\, \boldsymbol{G}_k^\top. \tag{9}$$

Finally, the estimated edge is generated by evaluating $\hat{r}_k = C(\hat{\boldsymbol{x}}_{k|k})$.

A 1-D edge detector provides the measurement residual $z_k = r_k - C(\hat{\boldsymbol{x}}_{k|k-1})$ from (4), which is obtained by processing the brightness values along the radius r_k emanating at angle θ_k. M number of candidate points ρ_i are selected based on the results of an edge detection function, and a probability distribution function describing the actual location of the edge is constructed from these points for each radius, using (7)–(9) from [15].

The modified Star–Kalman algorithm generates a sequence of state estimates of size $3N$ each time the vein contour is traversed, where θ_k takes values from 0 to 2π radians. The vein edge locations are described by the estimated $\hat{r}$. The estimation procedure is performed by consecutively traversing the contour several times, typically three. The original seed point is used throughout, and a new seed point is not calculated until the next image is processed. The state $\boldsymbol{x}_k$ is only initialized at $k = 0$, and data obtained from going around the contour once is used in consecutive traversals.

An ellipse centered at x_c, y_c is reconstructed using (1), with the estimated ellipse parameters $\hat{a} = \hat{a}_N$, $\hat{b} = \hat{b}_N$, $\hat{\phi} = \hat{\phi}_N$ in place of a, b, and ϕ. If the vein contour is approximated well by the ellipse, the approximate value of the transverse vessel area can be obtained from $\pi\hat{a}\hat{b}$.

The extracted contour $\hat{r}$ and the reconstructed ellipse are compared to each other, at additional computational expense, to insure smoothness for the contour $\hat{r}$. The root mean squared (rms) radial distance between boundaries $e_{r_{\rm rms}}$ [27] is used as an error measure, and is computed by measuring the distance between the estimated points $\hat{r}_k$ and the corresponding points on the generated ellipse. A data fit is deemed invalid if this error is larger than

$$\text{error threshold} = \max e_{r_{\rm rms}} = \sqrt{1.5 \cdot r_{\max}}\,. \tag{10}$$

This threshold was determined experimentally in [20], where it was first noted that $e_{r_{\rm rms}}/r_{\max}$ decreased as the search area decreased, as long as the feature was completely contained within the search area. This scaling is necessary because of the changes in the estimated ellipse parameters and contour points due to initial conditions, and allows a global threshold to be determined for varying search distances. Through additional experimentation it was found that results improved when using a threshold proportional to $\sqrt{r_{\max}}$. Larger threshold values allow better contour detection for less elliptically shaped features, but may also increase the mean error in the segmented contour. If a

data fit has been deemed invalid, $r_{\max}$ is decreased by 5%–7% of the initial value of $r_{\max}$ and the contour detection is repeated. If $r_{\max}$ reaches a predetermined lower bound (10%–13% of initial $r_{\max}$), contour detection has failed.

Additional processing in this stage includes the implementation of a median filter applied along each of the search radii in the modified Star–Kalman algorithm. This filter improves contour detection at a small computational cost when compared to comparable filters [20].

IV. Vessel Tracking

The initial seed point (x_{c_0}, y_{c_0}) within the vein employed in the spatial Kalman filter described above is entered manually by the operator by using a mouse or the ultrasound machine pointing device. Without updating the seed point, the vessel motion with respect to the ultrasound transducer causes the spatial Kalman filter to not converge and the vessel center is lost.

A seed tracking method was developed to accommodate feature motion, following the approach presented in [16]. The vein seed point (x_{c_i}, y_{c_i}) is estimated through successive image frames i by a temporal Kalman filter (it is assumed $z_{c_i} = 0$, as described below). For the Kalman filter dynamics, it is assumed that the vein center moves with constant velocity from frame to frame. If the current seed location is $\boldsymbol{x}_i = [x_i \;\; y_i \;\; z_i]^T$, the seed location in the next frame $\boldsymbol{x}_{i+1}$ is described by $\boldsymbol{x}_i$ and the previous seed location $\boldsymbol{x}_{i-1}$ using

$$\boldsymbol{x}_{i+1} = \boldsymbol{x}_i + \Delta \dot{\boldsymbol{x}}_i = \boldsymbol{x}_i + (\boldsymbol{x}_i - \boldsymbol{x}_{i-1}) \tag{11}$$

with the seed velocity $\dot{\boldsymbol{x}}_i$ described by $\dot{\boldsymbol{x}}_i = (\boldsymbol{x}_i - \boldsymbol{x}_{i-1})/\Delta$, and Δ is the discretization step. Typically, Kalman filters use measurements of the state at the current iteration to update the estimate, in this case the seed location. Unfortunately, a reliable measurement of the seed location at the current frame is not available. However, we do have the seed location at the previous frame, or a delayed measurement.

The state space description of this system with delayed measurements is written as

$$\begin{cases} \boldsymbol{X}_{i+1} = \mathbf{A}\,\boldsymbol{X}_i + \boldsymbol{\zeta}_i \\ \boldsymbol{u}_i = \mathbf{C}\,\boldsymbol{X}_i + \boldsymbol{\vartheta}_i \end{cases} \tag{12}$$

where

$$\mathbf{A} = \begin{bmatrix} 2\cdot\mathbf{I}_{3\times3} & -\mathbf{I}_{3\times3} \\ \mathbf{I}_{3\times3} & \mathbf{0}_{3\times3} \end{bmatrix}$$
$$\mathbf{C} = [\,\mathbf{0}_{4\times2} \;\; \mathbf{I}_{4\times4}\,]. \tag{13}$$

$\mathbf{I}_{n\times n}$ is the identity matrix, while $\mathbf{0}_{m\times n}$ is an m by n zero matrix. The state is defined by

$$\boldsymbol{X}_i = \begin{bmatrix} \boldsymbol{x}_i \\ \boldsymbol{x}_{i-1} \end{bmatrix} = [\,x_i \;\; y_i \;\; z_i \;\; x_{i-1} \;\; y_{i-1} \;\; z_{i-1}\,]^\top \tag{14}$$

$\boldsymbol{u}_i$ is the measurement of the seed point locations, and $\boldsymbol{\zeta}_i$ and $\boldsymbol{\vartheta}_i$ are assumed to be sequences of white, zero-mean, Gaussian process and measurement noise with known covariances, respectively. Note that the resulting dynamic system (12) is independent of the discretization step Δ.

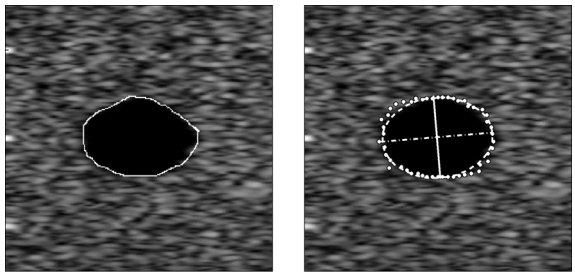

(a) Simulated Data (b) Simulated Data

Fig. 3. Examples of contour and parameter estimation. Simulated data used to test contour detection, with (a) expert tracing and (b) detected contour with detected contours (white circles). The estimated semi-major axis a and semi-minor axis b are presented as a solid and dashed line, respectively, oriented according to the estimated ϕ.

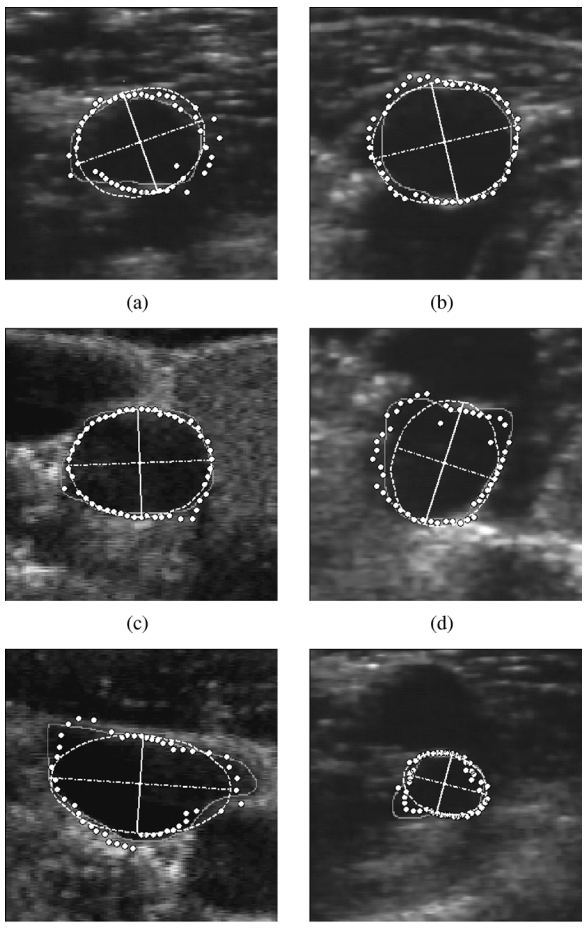

(a) (b) (c) (d) (e) (f)

Fig. 4. Patient data (images cropped to 200 × 200 pixels) with examples of detected contours (white circles) and estimated ellipses. The estimated semi-major axis a and semi-minor axis b are presented as a solid and dashed line, respectively, oriented according to the estimated ϕ. Expert tracings presented in grey.

The temporal Kalman filter trajectory describes the predicted spatial motion $\boldsymbol{s}$ of the vein center from frame to frame, as shown in Fig. 5, and the estimated seed point $\hat{\boldsymbol{x}}_i$ can be computed as described in [28]. The estimated point $\hat{\boldsymbol{x}}_i$ is calculated in the current image frame $\prod_i$, and then projected onto the plane of the ultrasound image, using only the $\hat{x}_i$ and $\hat{y}_i$ components (i.e., setting $\hat{z}_i = 0$). The 4×1 measurement vector $\boldsymbol{u}_i$ is composed

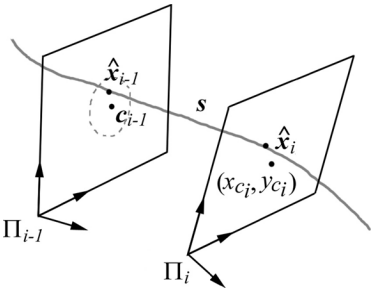

Fig. 5. Tracking the seed point. An estimate $\hat{x}_i$ of the vessel center (x_{c_i}, y_{c_i}) along trajectory $\mathbf{t}$ is calculated for each image plane Π_i using a constant velocity model. The previously obtained vessel center c_{i-1} is used as measurement.

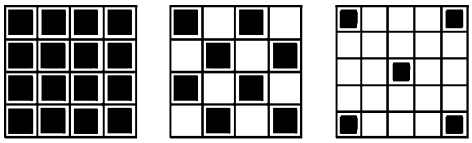

(a) Full mask (b) Half mask (c) Fifth mask

Fig. 6. The location with minimum brightness in an image region is found using the SAD and (a) all, (b) half, or (c) one-fifth of the pixels in the region.

of the centroid $\boldsymbol{c}_{i-1}$ of the contour detected at time $i-1$ as the measurement of $\boldsymbol{x}_{i-1}$, while the measurement of z_i is set to zero since $\hat{\boldsymbol{x}}_i$ should lie on Π_i. The location sensor measurements are used to compute the required coordinate systems transformations so that all coordinates are described in the current image frame Π_i.

The estimated seed location from the Kalman filter is adequate for most cases, with two notable exceptions. Since we assume the seed moves with constant velocity, the seed location may drift when imaging at one location (no movement) and cause the seed location to be lost. Also, large errors may occur when tracking the seed at one location (no movement) and suddenly moving, or when moving the probe and suddenly stopping. To address these issues, a subsampled SAD correlation is performed in the area surrounding the seed point $(\hat{x}_i\ \hat{y}_i)$ estimated by the temporal Kalman filter described above. By using a mask of size $0.8 \cdot r_{\max}$ with constant and equal pixel values, the location with minimum brightness (minimum SAD) is found, corresponding to the center of the vessel, and used as (x_{c_i}, y_{c_i}). The subsampling consists of using a fraction of all pixels, such as 1/2 or 1/5 of all pixels within the mask, as illustrated in Fig. 6, which reduces the correlation processing requirements without a noticeable decrease in accuracy. Results are presented in Section VI.

V. Validation Protocol

1) Contour Detection: The contour detection algorithm was evaluated in two steps. The first was to determine the accuracy of the algorithm for detecting ellipse parameters and contours from elliptical features with known characteristics, and the second step was to determine the accuracy with which the algorithm detected the actual feature contour determined by an expert tracing.

For the first step, ultrasound images were simulated using Field II [29], with elliptical features with known parameters, examples of which are shown in Fig. 3(a) and (b). The Field II package provides an excellent framework for simulating ultrasound images using linear acoustics [1], and has been used for various applications [30]–[32]. Nine different sets of ellipse parameters (eccentricity

$$e = \{0.0, 0.745, 0.866, 0.916, 0.943, 0.958, 0.968, 0.975, 0.979\}$$

and $\phi = 0°$ for all cases) were generated using 3.5 MHz as center frequency, 100 MHz sampling frequency, 192 elements (64 active elements) and 50 lines per image. The speed of sound was set to 1540 m/s, and data was compressed to show 60 dB of dynamic range. 80 000 scatterers were randomly generated for tissue, and their amplitudes were randomly set with normal distribution and maximum amplitude 1 as per typical Field II simulations. Amplitude was set to 0 inside the defined ellipses. In total, 18 simulated images were used (320×440 pixels, 0.091 mm/pix). Nine images as described above, and an additional 9 images with a 2 mm border, where the amplitude of the scatterers had a normal distribution and maximum amplitude 3.

The effect of noise on the accuracy of the algorithm was also explored by adding electrical noise (white, zero mean) to the simulated radio-frequency (RF) signals from which the simulated images were obtained. The resulting signal-to-noise ratios (SNR) for tissue regions in the B-mode images were approximately 40, 30, 20, 12, 5, and -3 dB, with lower SNR for the vessel regions. In addition, the effect of 2 dB/cm attenuation due to image depth was examined, by comparing results from images with and without attenuation. Images were simulated with different settings (7.0 MHz as center frequency, 40 MHz sampling frequency, 192 elements, 64 active elements, and 64 lines per image, other settings as above), with ellipses using the same eccentricity values as above and $\phi = \{-25°, 0°, 20°\}$, for a total of 25 images with and 25 without attenuation.

For the second step, six different vessels were segmented in three different ultrasound images: one image with the jugular vein and the common carotid artery (560×472 pixels), and two images each with one saphenous vein and arteries (720×480 pixels).

Three experts [one radiologist (Savvas Nicolaou) and two sonographers (Vicki Lessoway and Maureen Kennedy)] segmented all images by tracing the contour using an image editing application. Two of the experts (VL and MK) segmented all images twice, resulting in five expert tracings per image.

The algorithm was initialized in all cases with $N = 50$ radii, $\boldsymbol{Q} = \mathrm{diag}(2, 2, 0.1)$, $R = 20$, $M = 5$, and $\hat{\boldsymbol{x}}_{0|0} = [\, r_{\max}/2,\ r_{\max}/2,\ 0\,]^{\top}$. Values of $r_{\max}$ ranged from 60–80 pixels for simulated images and 70 to 85 pixels for patient images, depending on vessel size.

Seed points for each image were determined from the expert tracings, from which a central point was calculated as the mean of 50 evenly sampled points. The expert tracings were then defined in polar coordinates originating at this central point. A new contour was defined by dividing the radial component of each polar coordinate by 4. Pixels that were contained within this new contour were sampled by a factor of 4 and the resulting coordinates, all of which are unique and located roughly at the center

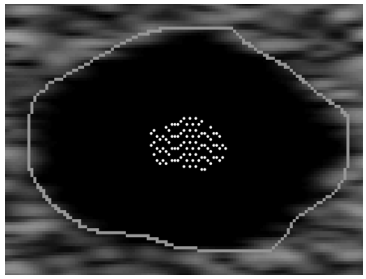

Fig. 7. Location of seed points. Example of seed points (.) generated for a simulated image. Expert tracing shown in gray.

TABLE I
OVERALL PARAMETER ESTIMATION RESULTS—SIMULATED IMAGES

	a (%)	b (%)	ϕ ($^\circ$)	FArea (%)	EArea (%)	MEr (pix)	RMSEr (pix)
Thresh. = $\sqrt{1.5 \cdot r_{max}}$, (n = 999)					(n = 4995)		
μ	-13.68	-2.20	0.80	-15.72	-8.14	-1.06	6.04
σ	8.52	19.89	19.14	16.67	18.03	2.10	2.16
Threshold = 6, (n = 799)					(n = 3995)		
μ	-12.44	-2.05	3.82	-14.46	-7.32	-1.00	5.94
σ	7.98	21.38	19.72	17.10	18.85	2.16	2.28

Mean (μ) and std. dev. (σ) of errors for ellipse parameters a, b, and area compared to πab (FArea) and expert tracings (EArea). Values of ellipse parameter ϕ, and mean MEr and rms RMSEr errors between contour and expert tracing.

of the vessel, were used as the seed points. Fig. 7 shows an example of seed points generated for a simulated image.

For simulated images, the estimated ellipse parameters were compared to the known parameters and errors were determined as a percentage of the known parameter. The area obtained from the estimated ellipse parameters using $\pi\hat{a}\hat{b}$ was compared to the "true" area, calculated from the known parameters using πab.

The area from estimated ellipse parameters was also compared to the area resulting from the expert tracing for all images. The expert area was determined by counting the pixels within the traced contours. These area errors are also reported as percentages of the "true" expert areas.

Errors between the detected contour and the expert contour were determined using the mean and rms radial distance between boundaries [27]. Given a seed point, along each of the N radii, the expert contour is found and the distance to the detected contour point for the corresponding radii is found. This measurement is used to determine mean (MEr) and rms (RMSEr) errors between true and detected contours.

Errors are presented in pixels in Section VI because scaling factors were known for simulated images (0.0625–0.0893 mm/pix), but not for the ultrasound images of patients. However, all vessel sizes were similar when measured in pixels, and ranged from ~ 100 pixels along their longest axis for simulated images, and ~ 80 to ~ 150 pixels for patient images. Because the intended application allows for a range of scaling factors, we believe results presented in pixels more accurately represent the performance of our segmentation method. However, image scaling factors should be taken into account when interpreting results for specific cases.

2) Vessel Tracking: The vessel tracking presented in Section IV was implemented and tested as follows. Three representative series of ultrasound images of 100 images each, where a feature from an ultrasound phantom was seen to move from left to right (a slow (S1), medium (S2), and fast (S3) step) were acquired and saved for offline evaluation, along with corresponding location data. The peak speeds were 1.6, 6.9, and 12.6 pixel/frame (1.4, 6.2, 11.2 mm/s at 10 Hz, respectively) along the x axis for the slow, medium, and fast steps, respectively. Movement along the y axis was considered negligible. The center of the features was determined manually, and the tracking algorithm was used to estimate the vessel centres using image and sensor data. An error measure was determined for each image by calculating the distance from the tracked position to the true segmented position.

The tracking method presented in (1) and (2) in [16] was also implemented and used as a baseline. This system also uses a constant velocity model, but the measurement consists of the current seed location obtained by projecting the previous centroid onto the current image frame. The state estimate is calculated in a single global reference frame. The estimated seed point was also corrected using the SAD correlation described above. It was found that this system does not work sufficiently well, as the seed location was repeatedly lost especially for faster movements, through the implementation of this model on a prototype of the DVT system from [23], and motivated the current tracking model.

The use of the subsampled SAD was also investigated by generating estimates of the vessel locations using the tracking algorithm from Section IV and three different settings for the SAD correlation as described in the same section. Errors between the true positions and tracked positions were calculated as above for each of the SAD settings. A two-tailed t test was used to determine whether there was any significant difference between the mean errors obtained from the tracked positions when using the different subsampled SAD settings.

VI. EXPERIMENTAL RESULTS

A. Contour Detection

In the first validation step a total 999 seed points were generated from the expert tracings of the 18 simulated ultrasound images and used as seed points for the algorithm, which was initialized, as described in Section V-A.I. The number of seed points per image ranged from 23 to 132, and were at most ± 13 pixels from the seed in the x direction and at most ± 13 pixels from the seed in the y direction. Each detected contour was compared to each of the five expert tracings and estimated ellipse parameters were compared to the known values used to simulate the images.

Results are divided into two categories, based on the error threshold presented in Section III, used to determine invalid data. The first category uses the value as defined in (10), while the second category uses a fixed value of six pixels. A valid result was obtained in 100% of evaluations of the algorithm when using (10) as the error threshold, and only in 80% of evaluations when using $\max e_{r_{\mathrm{rms}}} = 6$ pixels.

Overall results are presented in Table I, with mean (μ) errors and standard deviations (σ) for ellipse parameters a, b, and the area calculated from $\pi\hat{a}\hat{b}$ (FArea), expressed as a percentage of

TABLE II
DETECTED ELLIPSE PARAMETERS

a (pix)			b (pix)			ϕ (°)			FArea (pix^2)			n
True	μ	σ	True	μ	σ	True	μ	σ	True	μ	σ	
55	51.0	3.98	55	52.44	3.64	0	4.81	31.4	9503	8404	765	256
55	49.79	2.77	36.67	35.63	2.24	0	5.78	17.71	6336	5575	480	172
55	49.53	2.81	27.5	26.85	1.82	0	-1.70	11.34	4752	4189	476	125
55	46.11	2.37	22	20.67	1.17	0	-1.05	8.70	3801	2999	279	100
55	45.71	2.16	18.33	17.63	1.20	0	-2.71	7.44	3167	2537	270	93
55	43.28	1.97	15.71	15.84	4.88	0	-2.93	8.88	2715	2144	597	73
55	44.77	2.82	13.75	13.81	5.15	0	-2.30	8.80	2376	1948	727	69
55	41.77	2.92	12.22	14.64	5.72	0	-4.90	8.44	2111	1919	749	59
55	38.90	3.16	11	9.87	3.00	0	-3.86	5.37	1900	1198	313	52

Mean (μ) and std. dev. (σ) of estimated parameters a, b and ϕ, and area from $\pi\hat{a}\hat{b}$ (FArea) compared to true values, using $\text{threshold} = \sqrt{1.5 \cdot r_{\max}}$.

TABLE III
CONTOUR DETECTION RESULTS – SIMULATED IMAGES, ERRORS PER EXPERT, Validation threshold $= \sqrt{1.5 \cdot r_{\max}}$

	SN (n = 999)		VL (n = 1998)		MK (n = 1998)	
	μ	σ	μ	σ	μ	σ
EArea (%)	-10.12	17.54	-9.19	17.93	-6.11	18.19
MEr (pix)	-1.28	2.14	-1.35	2.09	-0.66	2.02
RMSEr (pix)	6.28	2.03	5.91	2.14	6.04	2.24

Mean (μ) and std. dev. (σ) of error from area compared to expert tracing (EArea), and mean MEr and rms RMSEr errors between contour and expert tracing, for each expert (SN = Savvas Nicolaou, VL = Vicki Lessoway, MK = Maureen Kennedy).

TABLE IV
CONTOUR DETECTION RESULTS—SIMULATED IMAGES, ERRORS PER EXPERT, Validation threshold $= 6$

	SN (n = 799)		VL (n =1598)		MK (n = 1598)	
	μ	σ	μ	σ	μ	σ
EArea (%)	-8.33	17.77	-8.78	18.89	-5.35	19.17
MEr (pix)	-1.06	2.16	-1.37	2.17	-0.60	2.09
RMSEr (pix)	6.14	2.14	5.84	2.26	5.93	2.38

Mean (μ) and std. dev. (σ) of error from area compared to expert tracing (EArea), and mean MEr and rms RMSEr errors between contour and expert tracing, for each expert (SN = Savvas Nicolaou, VL = Vicki Lessoway, MK = Maureen Kennedy).

the true known value. The mean and standard deviation of ϕ is also included. Also shown are μ and σ of the area error when compared to the expert tracings (EArea), as a percentage of the area of the expert tracing. Finally, the mean error (MEr) and the rms error (RMSEr) between the detected contour and expert tracing are presented. The sign indicates that areas were over- (+) or underestimated (−).

It should be noted that the sample number is 5 times the number of generated seed points for errors obtained when comparing the algorithm results to expert tracings (EArea, MEr, RMSEr), since each detected contour was compared to each of the five expert tracings.

Table II presents the mean (μ) and standard deviation (σ) of ellipse parameters and the resulting ellipse area obtained by our algorithm, compared to the true known values.

The EArea, MEr, and RMSEr errors for individual experts from the simulated images are presented in Tables III and IV. Data has been subdivided as described above, with data obtained when the validation threshold is as in (10) in Table III, and when the validation threshold $= 6$ pixels in Table IV.

The results of contour detection and parameter estimation on noisy images are shown in Table V. The same 999 seed points, as described above were used. The error distributions obtained from noisy data were compared to those from noiseless images using a two-sample Kolmogorov–Smirnov goodness-of-fit hypothesis test with a significance level of $\alpha = 0.05$. While a statistically significant difference was found for the mean contour error, MEr (p-value = 0.0388), and the estimated ellipse angle, ϕ (p-value = 0.0409), at SNRs of 30 and 12 dB, results remain very similar to those obtained from the noiseless data until the SNR approaches 0 dB. P-values for all measures are less than 0.05 when SNR is -3 dB.

Table VI shows algorithm results from 1375 seed points on images with and without attenuation. As with noisy data, the error distributions from both sets were compared to using the two-sample Kolmogorov–Smirnov goodness-of-fit hypothesis test with a significance level of $\alpha = 0.05$. Parameter estimation errors were found to be significantly different (p-values$<$ 0.0182) from results without attenuation, with error differences of less than 4%.

The objective of the second validation step was to compare the results of the feature detection algorithm to the expert segmentation in the patient images. Expert tracings were again used to generate a total of 564 seed points, and the feature detection algorithm was again initialized, as described in Section III. The number of seed points per image ranged from 37 to 144, and were at most ± 21 pixels from the seed in the x direction and at most ± 12 pixels from the seed in the y direction. Again, each contour was compared to five expert tracings, generating $5n = 2820$ total measurements.

The mean (MEr) and rms (RMSEr) radial distance between the detected boundaries and the expert boundaries was determined in pixels, and the differences between expert area and the area from the estimated ellipse parameters (EArea) was determined as a percentage of the expert area. These results are presented in Table VII.

As in the first step, the same two validation thresholds were used for the patient images dataset. Table VIII shows errors for individual experts when the validation threshold is as in (10) with a 100% validation rate, and Table X shows errors for individual experts when the validation threshold $= 6$ pixels with

TABLE V
PARAMETER ESTIMATION AND CONTOUR DETECTION RESULTS FOR IMAGES WITH VARYING SNRS

SNR (dB)	a (%)		b (%)		ϕ (°)		FArea (%)		EArea (%)		MEr (pix)		RMSEr (pix)	
	μ	σ	μ	σ	μ	σ	μ	σ	μ	σ	μ	σ	μ	σ
–	-13.68	8.52	-2.20	19.89	0.80	19.14	-15.72	16.67	-8.14	18.03	-1.06	2.10	6.04	2.16
40	-13.95	8.74	-2.74	17.76	-0.77	19.43	-16.38	15.93	-8.88	17.07	-1.17	1.88	6.01	2.00
30	-14.06	8.58	-2.53	17.49	0.01	19.58	-16.37	14.65	-8.83	16.20	-1.16	1.82	6.03	2.00
20	-13.98	8.58	-2.61	16.68	-1.39	19.47	-16.28	14.99	-8.84	15.01	-1.14	1.90	6.03	2.03
10	-14.01	8.76	-2.92	12.79	-0.77	19.43	-16.46	13.52	-9.06	13.28	-1.14	1.68	5.98	1.90
5	-14.73	9.54	-0.54	27.45	0.91	19.13	-15.64	20.39	-8.15	21.59	-1.13	2.53	6.28	2.60
-3	-18.25	14.31	-7.88	25.29	-1.35	20.42	-23.46	24.16	-17.09	24.93	-2.56	4.61	7.45	4.59

TABLE VI
PARAMETER ESTIMATION AND CONTOUR DETECTION RESULTS FOR IMAGES WITH ATTENUATION

Att. (dB/cm)	a (%)		b (%)		ϕ (°)		FArea (%)	
	μ	σ	μ	σ	μ	σ	μ	σ
–	-22.2	12.3	-2.4	26.7	-1.1	13.0	-25.1	16.6
2	-21.7	11.3	-6.7	18.5	0.8	12.9	-27.2	12.6

TABLE VII
OVERALL RESULTS—PATIENT IMAGES

	EArea (%)	MEr (pix)	RMSEr (pix)
Thresh. = $\sqrt{1.5 \cdot r_{max}}$ (n = 2820)			
μ	11.66	1.06	10.47
σ	28.19	5.83	4.53
Threshold = 6, (n = 1835)			
μ	13.24	1.70	10.09
σ	23.98	5.17	4.30

Mean (μ) and std. dev. (σ) of error from area compared to expert tracing (EArea), and mean MEr and rms RMSEr errors between contour and expert tracing, from patient images ranging from 560 × 472 to 720 × 480 pixels.

TABLE VIII
CONTOUR DETECTION RESULTS—PATIENT IMAGES, ERRORS PER EXPERT, Validation threshold = $\sqrt{1.5 \cdot r_{\max}}$

	SN (n = 564)		VL (n =1128)		MK (n = 1128)	
	μ	σ	μ	σ	μ	σ
EArea (%)	5.95	27.26	7.62	25.72	18.55	29.58
MEr (pix)	0.64	6.13	0.31	5.74	2.03	5.63
RMSEr (pix)	11.03	4.82	10.52	4.58	10.13	4.29

Mean (μ) and std. dev. (σ) of error from area compared to expert tracing (EArea), and mean MEr and rms RMSEr errors between contour and expert tracing, for each expert (SN = Savvas Nicolaou, VL = Vicki Lessoway, MK = Maureen Kennedy).

TABLE IX
OVERALL RESULTS, IN PIXELS— PATIENT IMAGES

EArea (pix^2)				n	Image (Fig. 4)
True	μ	σ	V		
4862	6488	1572	0.24	135	(a)
7113	8532	435	0.05	420	(b)
7172	6782	272	0.04	495	(c)
6546	8528	810	0.09	360	(d)
6240	6731	1020	0.15	380	(e)
2514	2113	1697	0.80	45	(f)

Mean (μ), std. dev. (σ) and coefficient of variation (V) of estimated area (EArea) compared to True value from expert tracing, using validation threshold = 6.

TABLE X
CONTOUR DETECTION RESULTS -PATIENT IMAGES, ERRORS PER EXPERT, Validation threshold = 6.

	SN (n = 367)		VL (n =734)		MK (n = 734)	
	μ	σ	μ	σ	μ	σ
EArea (%)	9.14	24.20	9.45	21.07	19.08	25.40
MEr (pix)	1.47	5.55	0.97	4.92	2.56	5.10
RMSEr (pix)	10.69	4.59	10.16	4.28	9.72	4.14

Mean (μ) and std. dev. (σ) of error from area compared to expert tracing (EArea), and mean MEr and rms RMSEr errors between contour and expert tracing, for each expert (SN = Savvas Nicolaou, VL = Vicki Lessoway, MK = Maureen Kennedy).

a 65% validation rate. Examples of the results of the feature detection algorithm and parameter estimation on simulated and human data are presented in Fig. 4.

The mean (μ) area values for the patient images are also presented in Table IX, alongside the standard deviation (σ), the coefficient of variation V (ratio of standard deviation to mean), and the "True" expert values, obtained when using a validation threshold of 6 pixels. The patient images are shown in Fig. 4. It is observed that the smallest V was obtained from a more elliptically shaped vessel [Fig. 4(c)]. The largest V was obtained from the image with the smallest feature [Fig. 4(f)], which may explain the large variation. While μ is close to the true value, σ for this image was the largest of all.

The computation time was on the order of 10 ms for each estimation when tested using Matlab on a modern PC and unoptimized code. The significance of this is discussed in Section VII.

B. Seed Tracking

The tracking method from Section IV was implemented using an 80 pixel subsampled SAD, with 1/5 pixels within the mask (see Fig. 6). The method from [16] was implemented using an 80 pixel mask. The tracking results with errors are presented in Fig. 8. For slower movements, both implemented tracking methods are seen to work appropriately [Fig. 8(a)], but for larger movements [Fig. 8(c) and (d)], only our method with delayed location measurements can track the seed location, as shown by the data.

For the subsampled SAD validation, the slow (S1) and medium (S2) step ultrasound image series were used, and the algorithm was implemented using a 80 pixel square mask, using all, 1/2 and 1/5 the pixels within the mask. Typical results are presented in Fig. 9. The errors between the tracked points

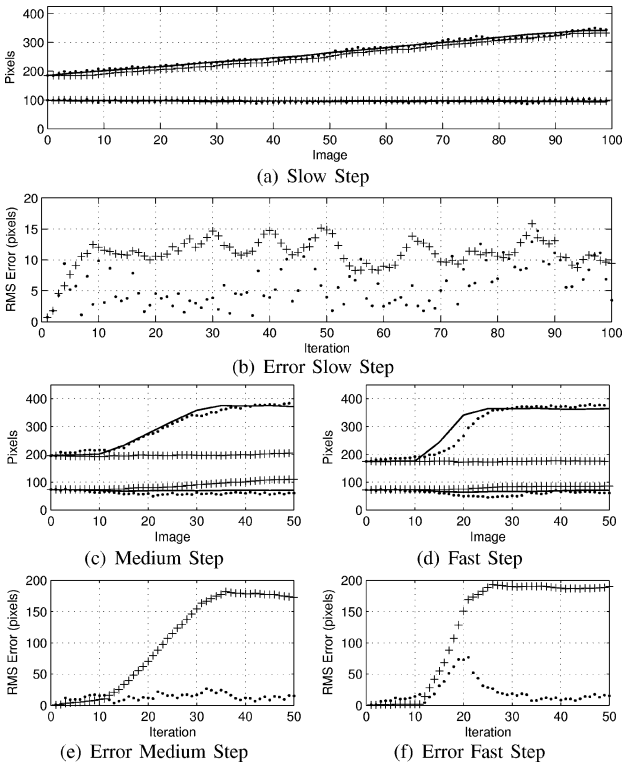

Fig. 8. Seed tracking results. A seed point was tracked in a (a) slow, (c) medium, and (d) fast step. Manual segmentation is represented by the solid line, the previous tracking method by (+) and the method presented herein by (.), and the x (above) and y (below) coordinates are presented. Errors for the (b) slow, (e) medium, and (f) fast steps are also shown.

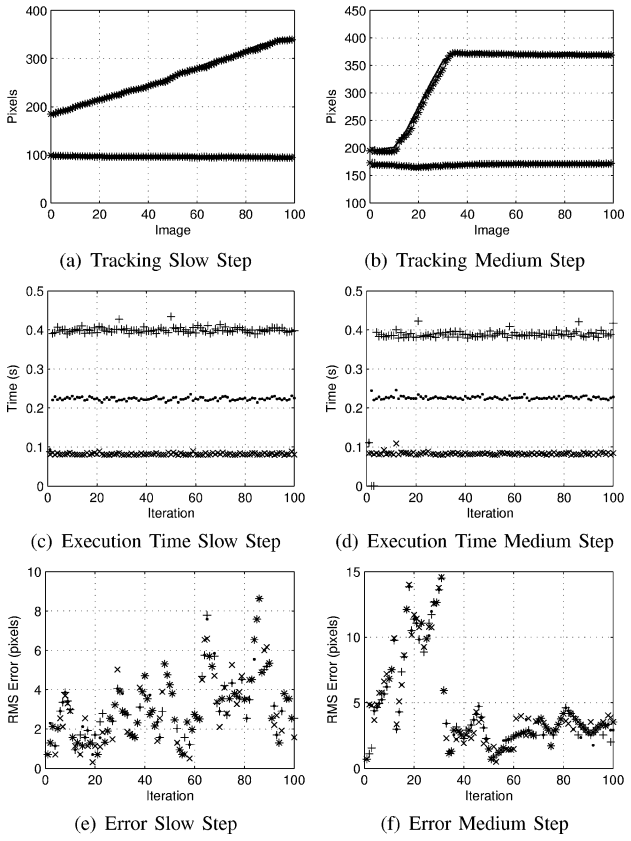

Fig. 9. SAD Validation. A seed point was tracked in a (a) slow and (b) medium step, using all (+), half (·), and one-fifth the pixels (x). Execution times per image for the (c) slow and (b) medium step are presented, as well as (e), (f) respective errors.

and the true location are presented in Table XI. No statistically significant difference between the SAD methods was found, while a reduction in execution time proportional to the number of pixels used can be clearly observed.

VII. Discussion

It has been demonstrated that the contour detection and parameter estimation algorithm presented in this paper can identify ellipse parameters with mean errors ranging from $\sim 2\%$ to $\sim 13\%$, and can detect contours that correspond to expert tracings. The estimated contour area also correlates to the true transverse area as determined by the experts, allowing the quick and parametric calculation of area of elliptical features. Even when features are slightly nonelliptical, area calculations reflect true values when using this algorithm, as seen by the moderately low mean area values in Table X. This may be due to the over- and underestimation of the ellipse parameters at different locations on the contour, which result in an ellipse with similar area to that of the vessel. Furthermore, mean errors between the detected contour and expert tracing are low. Results across experts also are consistent.

Our method performs well when compared to other contour detection methods. When comparing the detected contour to expert tracings, we have obtained a mean error of -1.0 pixels with a standard deviation of 2.16 pixels on simulated images, and a mean error of 1.7 pixels with a standard deviation of 5.17 pixels on patient images. For example, [17] reports a mean

TABLE XI
Errors and Execution Time for Different SAD Sizes

	Err. S1 (pix)		Err. S2 (pix)		Exec. Time (s)	
	μ	σ	μ	σ	μ	σ
Full mask	4.539	3.423	3.082	1.574	0.388	0.049
Half mask	4.595	3.383	3.059	1.599	0.224	0.013
Fifth mask	4.625	3.435	3.010	1.705	0.082	0.003

Mean (μ) and std. dev. (σ) of errors from tracking a vessel center in a slow (S1) and a medium (S2) step images series when using all, half, and one-fifth the pixels in a subsampled SAD mask. Execution time is also shown.

error of 2.98 pixels with a standard deviation of 3.79 pixels, detecting features ranging from 6.7–10.7 mm and scaling factors of 0.067 mm/pix, very similar to those in our DVT screening system. While our method is more variable, the trade-off is greatly increased processing time, as discussed below. Slightly better results are obtained as the validation threshold defined in (10) is lowered. While there is some variability in the results, by observing the standard deviation in Table I, this should be reduced when used in conjunction with a tracking algorithm. Also, some error may have been introduced into the ellipse parameter measurements because of the possible "rotation" of the results if a and b are switched and ϕ rotated by $\pm 90°$. Additionally, the result is expressed as a percentage of the true value, yet it can be seen in Table II that the standard deviation of both a and b are quite similar, and are not more than six pixels ($\sim 10\%$ of the maximum feature dimension). Moreover, our contour detection

algorithm has been proven to perform reliably over a range of SNRs, as consistent results were obtained for tissue SNRs between 40–12 dB. Indeed, statistically significant differences of all error measures are not found until the magnitude of the noise approaches the magnitude of the signal ($\mathrm{SNR} = 0\,\mathrm{dB}$). Typical expected SNRs range from 60 to 40 dB for tissue in B-mode images.

While all results obtained from images with attenuation are significantly different from those obtained from images without attenuation, the differences between mean errors are very small ($< 4\%$), and in the case of the ellipse angle ϕ the error is reduced. Additionally, the spread of all errors are also reduced. This variation in parameter estimation is acceptable for the current application.

The large variation in ϕ can be explained by the two circular images used ($e = 0$), as in these cases ϕ can take any value. When removing these images from the dataset, the mean value of ϕ is $-3.26°$ with standard deviation of 10.78°, when using $\max\ e_{r_{\mathrm{rms}}} = 6$ and $\mathrm{n} = 546$. This variation can further be reduced by taking the mean value of ϕ over all k, resulting in a mean value of $-2.16°$ and standard deviation of 5.13° ($\max\ e_{r_{\mathrm{rms}}} = 6$, $\mathrm{n} = 738$).

In the DVT screening system presented in [23], results from the contour detection from the previous frame are used to initialize the current frame. While this was not included in the current validation, it has been observed that the contour detection is stable over successive frames obtained at the same location. Future work could include an evaluation of the reliability of the contour detection with data from previous frames compared to standard initial conditions.

Even though the transverse area values are variable, the algorithm is still adequate for the intended application, the DVT screening system described in [20] and [23].

While chronic clots may be more echogenic, younger clots are more likely to have echogenicity similar to that of blood [33]. The manner in which clots are located using the CUS method also supports this observation. The system in which the contour detection and tracking is implemented is aimed at screening patients at risk of DVT for new thrombi, not chronic thrombi, as immediate medical treatment is important in avoiding DVT complications [33]–[35].

The seed tracking method shows promising results. While typically template matching has been used to track a feature over successive frames, we have modified this concept for determining the location of minimum brightness. SAD correlation has previously been identified as a good method for determining correlation between ultrasound image data and a mask [22]. Our method has addressed the issue of high processing time, and we show that the use of subsampled SAD in conjunction with the tracking greatly decreases execution time, without any noticeable decrease in tracking accuracy. We have also shown an improvement over previous tracking systems that use Kalman filters [15].

The main drawback of this tracking implementation is sensitivity to location measurements. First, location sensor noise may adversely affect tracking accuracy. Second, because of the distance from the sensor to the actual image plane location, small orientation errors may be translated into large errors. Even so, preliminary results show that the inclusion of location measurements greatly enhances the seed tracking capability of the system, and any deterioration because of measurement noise is greatly outweighed by the ability of tracking fast movements.

The authors are aware that the presence of metals has to be accounted for through calibration of the location sensor (the ultrasound transducer shell is made of aluminum). The accuracy was tested using a qualitative evaluation on known phantoms and was found to be sufficient for it not to interfere with our application.

The execution time results for both contour detection and tracking are encouraging and more than adequate for real-time implementation. Moreover, our mean segmentation time of $\sim 23\ \mathrm{ms}$ is much lower than other segmentation methods (for example, [17] reports 0.8 s for 128×128 images, on a Pentium II 300 MHz computer).

Currently patient movement cannot be accounted for by the system. This, as well as other sources such as arterial pulse, are other possible sources of error.

Improvements to the feature detection and tracking algorithm are underway. Since the feature disappears from the image under compression, it cannot be detected. Therefore, quick recovery from losing the vein tracking following full compression is important, in order to avoid frequent operator intervention for seed initialization. Compounding or averaging the detected contours may lead to smaller errors and variations.

VIII. Conclusion

A vessel segmentation and tracking method for identifying vessel contours and transverse areas in ultrasound images have been presented. The vessel segmentation uses an extended Kalman filter and an elliptical vessel model to determine the vessel boundary and estimate ellipse parameters for that vessel, which can be used to quickly calculate the transverse area. A tracking method, which uses location measurements from a sensorized ultrasound probe, is implemented using a temporal Kalman filter to track the vessel location in real-time over image sequences.

The vessel segmentation and tracking were evaluated using simulated and patient data, and compared to expert tracings to determine accuracy. Results are encouraging and the segmentation and tracking have been implemented in a proposed deep vein thrombosis screening system, currently under clinical evaluation.

Acknowledgment

The authors would like to thank A. Hope and M. Kennedy for their collaboration with image segmentation and data collection.

References

[1] J. A. Noble and D. Boukerroui, "Ultrasound image segmentation: A survey," *IEEE Trans. Med. Imag.*, vol. 25, no. 8, pp. 987–1010, Aug. 2006.

[2] F. A. Anderson *et al.*, "A population-based perspective of the hospital incidence and case-fatality rates of deep vein thrombosis and pulmonary embolism. The worcester DVT study," *Arch. Intern. Med.*, vol. 151, pp. 933–938, 1991.

[3] M. C. H. Janssen, H. Wollersheim, I. R. O. Novakova, F. M. J. Heystraten, W. N. J. C. van Asten, and T. Thien, "Diagnosis of deep vein thrombosis: An overview," *Neth. J. Med.*, vol. 48, pp. 109–121, 1996.

[4] M. Atri, M. J. Herba, C. Reinhold, C. Leclerc, S. Ye, F. F. Illescas, and P. M. Bret, "Accuracy of sonography in the evaluation of calf deep vein thrombosis in both postoperative surveillance and symptomatic patients," *Am. J. of Roentgenol.*, vol. 166, pp. 1361–1367, 1996.

[5] J. J. Cronan *et al.*, "Deep venous thrombosis: US assessment using vein compression," *Radiology*, vol. 162, pp. 191–194, 1987.

[6] J. J. Cronan, G. S. Dorfman, and J. Grusmark, "Lower-extremity deep venous thrombosis: Further experience with and refinements of US assessment," *Radiology*, vol. 168, pp. 101–107, 1988.

[7] B. W. Frazee, E. R. Snoey, and A. Levitt, "Emergency department compression ultrasound to diagnose proximal deep vein thrombosis," *J. Emergency Med.*, vol. 20, no. 2, pp. 107–111, 2001.

[8] "The diagnostic approach to acute venous thromboembolism. Clinical practice guideline," *Am. J .Respir. Crit. Care Med.*, vol. 160, no. 3, pp. 1043–1066, 1999.

[9] N. Perone *et al.*, "Comparison of four strategies for diagnosing deep vein thrombosis: A cost-effectiveness analysis," *Am. J. Med.*, vol. 110, no. 1, pp. 33–40, 2001.

[10] J. Cornuz, S. D. Pearson, and J. F. Polak, "Deep venous thrombosis: Complete lower extremity venous US evaluation in patients without known risk factors—Outcome study," *Radiology*, vol. 211, pp. 637–641, 1999.

[11] S. M. Schellong *et al.*, "Complete compression ultrasonography of the leg veins as a single test for the diagnosis of deep vein thrombosis," *Thromb Haemost*, vol. 89, no. 2, pp. 228–234, 2003.

[12] B. Wolf, D. M. Nichols, and J. L. Duncan, "Safety of a single duplex scan to exclude deep venous thrombosis," *Br. J. Surg.*, vol. 87, no. 11, pp. 1525–1528, 2000.

[13] M. Kass, A. Witkin, and D. Terzopoulos, "Snakes: Active contour models," *Int. J. Comput. Vision*, pp. 321–331, 1988.

[14] D. Terzopoulos and R. Szeliski, "Tracking with Kalman snakes," in *Active Vision*, A. Blake and A. Yuille, Eds. Cambridge, MA: MIT Press, 1992.

[15] P. Abolmaesumi, S. E. Salcudean, W. H. Zhu, M. R. Sirouspour, and S. P. DiMaio, "Image-guided control of a robot for medical ultrasound," *IEEE Trans. Robot. Automat.*, vol. 18, no. 1, pp. 11–23, Feb. 2002.

[16] P. Abolmaesumi, M. R. Sirouspour, and S. E. Salcudean, "Real-time extraction of carotid artery contours from ultrasound images," in *Proc. 13th IEEE Symp. Comput.-Based Med. Syst.*, 2000, pp. 181–186.

[17] F. Mao, J. Gill, D. Downey, and A. Fenster, "Segmentation of carotid artery in ultrasound images: Method development and evaluation technique," *Med. Phys.*, vol. 27, no. 8, pp. 1961–1970, 2000.

[18] C. Chen, T. Poepping, J. Beech-Brandt, S. Hammer, R. Baldock, B. Hill, P. Allan, W. Easson, and P. Hoskins, "Segmentation of arterial geometry from ultrasound images using Balloon models," in *IEEE Int. Symp. Biomed. Imag.: Macro Nano*, Apr. 2004, vol. 2, pp. 1319–1322.

[19] N. Friedland and D. Adam, "Automatic ventricular cavity boundary detection from sequential ultrasound images using simulated annealing," *IEEE Trans. Med. Imag.*, vol. 8, no. 4, pp. 344–353, Dec. 1989.

[20] J. Guerrero, "Improved interface for deep venous thrombosis screening using B-mode ultrasound," M.S. thesis, Univ. British Columbia, Vancouver, BC, Canada, 2002.

[21] B. H. Friemel, L. N. Bohs, and G. E. Trahey, "Relative performance of two-dimensional speckle-tracking techniques: Normalized correlation, non-normalized correlation and sum-absolute-difference," in *Proc. IEEE Ultrason. Symp.*, Nov. 1995, vol. 2, pp. 1481–1484.

[22] C. M. Gallippi, L. N. Bohs, M. Anderson, A. Congdon, and G. E. Trahey, "Lateral blood velocity measurement in the carotid artery via speckle tracking," in *Proc. IEEE Ultrason. Symp.*, 2001, vol. 2, pp. 1451–1455.

[23] J. Guerrero, S. E. Salcudean, J. A. McEwen, B. A. Masri, and S. Nicolaou, "System for deep venous thrombosis detection using objective compression measures," *IEEE Trans. Biomed. Eng.*, vol. 53, no. 5, pp. 845–854, May 2006.

[24] A. Fenster and D. B. Downey, "3-D ultrasound imaging: A review," *IEEE Eng. Med. Biol. Mag.*, vol. 5, pp. 41–51, Nov./Dec. 1997.

[25] S. W. Hughes, T. J. D'Arcy, D. J. Maxwell, W. Chiu, A. Milner, J. E. Saunders, and R. J. Sheppard, "Volume estimation from multiplanar 2-D ultrasound images using a remote electromagnetic position and orientation sensor," *Ultrasound Med. Biol.*, vol. 22, no. 5, pp. 561–572, 1996.

[26] Y. Bar-Shaloom and T. E. Fortmann, *Tracking and Data Association*. New York: Academic, 1988.

[27] V. Chalana and Y. Kim, "A methodology for evaluation of boundary detection algorithms on medical images," *IEEE Trans. Med. Imag.*, vol. 16, no. 5, pp. 642–652, Oct. 1997.

[28] Y. Bar-Shalom, X. R. Li, and T. Kirubarajan, *Estimation with Applications to Tracking and Navigation*. New York: Wiley, 2001.

[29] J. A. Jensen, "Field: A program for simulating ultrasound systems," *Med. Biol. Eng. Comput.*, vol. 34, pt. 1, pp. 351–353, 1996.

[30] M. J. Ledesma-Carbayo, J. Kybic, M. Desco, A. Santos, M. S'uhling, P. Hunziker, and M. Unser, "Spatio-temporal non-rigid registration for ultrasound cardiac motion estimation," *IEEE Trans. Med. Imag.*, vol. 24, no. 9, pp. 1113–1126, Sep. 2005.

[31] P. Hassenpflug, R. W. Prager, G. M. Treece, and A. H. Gee, "Speckle classification for sensorless freehand 3-D ultrasound," *Ultrasound Med. Biol.*, vol. 31, no. 11, pp. 1499–1508, Nov. 1998.

[32] D. Boukerroui, O. Basset, A. Baskurt, and G. Gimenez, "A multiparametric and multiresolution segmentation algorithm of 3-D ultrasonic data," *IEEE Trans. Ultrason., Ferroelect., Freq. Contr.*, vol. 48, no. 1, pp. 64–77, Jan. 2001.

[33] S. Y. Emelianov, X. Chen, M. O'Donnell, B. Knipp, D. Myers, T. W. Wakefield, and J. M. Rubin, "Triplex ultrasound: Elasticity imaging to age deep venous thrombosis," *Ultrasound Med. Biol.*, vol. 28, no. 6, pp. 757–767, 2002.

[34] A. Mumme, W. Heinen, B. Geier, W. Maatz, L. Barbera, and G. Walterbusch, "Regional hyperthermic fibrinolytic perfusion after unsuccessful venous thrombectomy of extensive deep venous thrombosis," *J. Vasc. Surg.*, vol. 36, no. 6, pp. 1219–1224, Dec. 2002.

[35] S. Aglyamov, A. R. Skovoroda, J. M. Rubin, M. O'Donnell, and S. Y. Emelianov, "Model-based reconstructive elasticity imaging of deep venous thrombosis," *IEEE Trans. Ultrason., Ferroelect., Freq. Contr.*, vol. 51, no. 5, pp. 521–531, May 2004.